Large-scale ultra-fast strain engineering of CVD-grown two-dimensional materials on strain self-limited deformable nanostructures towards enhanced field effect transistors

Zheng Huang [a], Nan Lu [c], Zifeng Wang [a], Shuoheng Xu [a], Jie Guan [c], Yaowu Hu [a,b*]

[a] The Institute of Technological Sciences, Wuhan University, Wuhan, 430072, China

[b] School of Power and Mechanical Engineering, Wuhan University, Wuhan 430072, China

[c] School of Physics, Southeast University, Nanjing 211189, China

Abstract

Strain engineering of 2D materials is capable of tuning the electrical and optical properties of the materials without introducing additional atoms. However, there are still great challenges in realizing straining of 2D materials with CMOS compatibility. Here, a method for large-scale ultrafast strain engineering of CVD-grown 2D materials is proposed. We introduce locally non-uniform strains through the cooperative deformation of materials and metal/metal oxide core/shell nanoparticles through cold laser shock. Raman and PL spectra reveal that the tensile strain of MoS_2 changes and the band gap decreases after laser shock. MD simulations are used to investigate the mechanism of the ultrafast straining of CVD-grown 2D materials. Field effect transistors of CVD MoS_2 were fabricated, and the performances before and after straining of the same devices are compared. By adjusting the strain level of MoS_2, the field effect mobility can be increased from 1.9 $cm^2V^{-1}s^{-1}$ to 44.1 $cm^2V^{-1}s^{-1}$. This is the maximum value of MoS_2 FETs grown by CVD with SiO_2 as dielectric. As an environment-friendly, large-scale and ultra-fast manufacturing method, laser shock provides a universal strategy for large-scale adjustment of 2D materials strain, which will help to promote the manufacturing of 2D nano electronic devices and optoelectronic devices.

The physical properties of most materials can be widely adjusted by strain engineering[1–4]. Among them, the strain engineering of two-dimensional(2D) materials is particularly exciting because individual atomic layer sheets are inherently capable of withstanding greater mechanical strain than their monolithic materials or conventional electronic materials[5,6]. In 2D materials, strain changes the configuration of atomic bonds (length, angle and strength) and the interaction between electron orbitals, which in turn can control the properties of two-dimensional materials and provide a rich library for advanced applications.

Typical straining techniques include strain transferring from flexible or stretchable or bendable substrates[7–9], MEMS stretching[10–12], sphere diameter engineering[13], and nanoscale surface morphology regulating[14–17]. Among them, only the method nanoscale surface morphology regulating is CMOS compatible and electrical field effect transistors can be fabricated. However, current surface morphology regulations are typically based on rigid surface structures defined by high-resolution lithography or chemical means, which are typically difficult to fabricate accurately in large scale or when multiple layers are encountered[18,19]. 2D materials on these nanoscale features can be strained on these nano-features through chemical solutions filling and vaporization[20,21], but the residue would be detrimental to the transistor. Transferred 2D crystals on these nanoscale features can be strained by the weak van der Waals interactions between the substrate and the material, and it was shown that peeled samples on nanofeatures less than 2 nm show tremendous improvements in terms of device mobility[22,23]. The feature size is on the order of the materials' thickness (~ 1 nm) in this case. However, for large-scale applications, CVD-grown 2D materials with non-uniform wrinkles (tens of nanometers) and defects are more practical[14,24–26]. These wrinkles would easily relax the strains on nanofeatures at 2 nm scale, and increasing the aspect ratio of such features would break the 2D materials very easily, cutting off the current flow.

Conformability of 2D materials on surface features at tens of nanometers scale has been widely studied[17,27,28]. It is generally believed that the strain value is established due to the balancing between strain energy and adhesion potential of the material within a certain geometrical scale. In this slow and self-balancing case, wrinkles of CVD-grown relax the elastic strains, making the elastic strains difficult to build up and control.

Ultrafast straining by using a shock pressure induced during laser ablation has been studied recently. The ultra-high strain rate deformation capability prevents excessive self-relaxation of the wrinkles[29–33]. Nanowires and 2D materials were strained previously by using hard rigid SiO_2 nanofeatures defined by electron beam lithography, the method of which benefits the fabrication of FET devices, but is too costly and easily generates geometrical stress concentrators, breaking the device[30,34]. Polymer cushion layer was used to tackle this issue but the charging effect of the polymer is detrimental to the device performance[29]. Thus, for CVD-grown 2D materails, large-scale ultrafast straining at low cost and high efficiency with good controllability has not yet been demonstrated.

In this paper, we demonstrate the strain engineering of 2D materials on SiO_2/Si substrates of strain self-limited deformable metal@metal oxide nanoparticles (M@MO NPs) by laser shock induced cooperative deformation (LSICD). This process can modulate the strain of MoS_2 by laser shock induced cooperative deformation of metal nanoparticles and MoS_2 on rigid substrates, and change its band structure. Field effect transistors based on MoS_2 grown by CVD were fabricated, and the highest field effect mobility is obtained in low-k dielectrics for CVD MoS_2. This contamination-free and ultra-fast opto-mechanical nanomanufacturing method provides a universal strategy for large-scale adjustment of 2D materials strain, which can lead to the further development of high-performance electronic and mechanical electronic equipment in the future.

Results and Discussion

Laser shock treatment of 2D materials on rigid surface structures breaks the material at the stress concentration point, as shown in Fig. S1. The molecular dynamics (MD) simulation results revealed that during the laser shock process, the 2D materials were subjected to huge stress at the turning point of the mold, resulting in the destruction of its lattice structure, defects or fractures (shown in Fig. S1(a-b)). It can be seen from the SEM images of the samples that the 2D materials shocked on the rigid substrates would cause irreparable damage under impact pressure, which would reduce the electrical and optical properties of the materials.

Here, we further develop a method to produce large-area non-uniform strain in two-dimensional materials, as shown in Fig. 1(a). The 2D materials were transferred to SiO_2/Si substrates pre-deposited with nanoparticles by PMMA assisted transfer, and then subjected to laser shock treatment. Due to the non-uniform size of nanoparticles on the substrate surface, the transferred 2D materials were supported like a tent by nanoparticles, resulting in local strain. In fact, as reported by Garaj et al.[23], 2D materials transferred to the rough substrate might produce strains, which depended entirely on the roughness of the substrates and could not be adjusted effectively. However, we show here that the strain adjustment of 2D materials can be realized by high strain rate deformation induced by laser shock. Specifically, after the high energy density nanosecond laser beam was focused on the graphite surface, plasma would be generated, and the recoil momentum of the plasma would produce pulse pressure[35]. The gap between the 2D materials and SiO_2/Si substrates decreased in an ultrafast fashion, which eliminated strain relaxation due to wrinkles and increased the local strain of 2D materials during LSICD (as shown in Fig. 1(b)). In this method, nanoparticles could be formed by sputtering or directly spin coating without cumbersome lithography process, which was scalable for large-area and roll-to-roll manufacturing. In the meantime, the cooperative deformation of metal nanoparticles also avoided the occurrence of defects or fractures caused by stress beyond the strain limit of the 2D materials. Laser processing also had the advantages of high production efficiency, reliable quality and economic benefits, and is easy to integrate with the existing semiconductor manufacturing process.

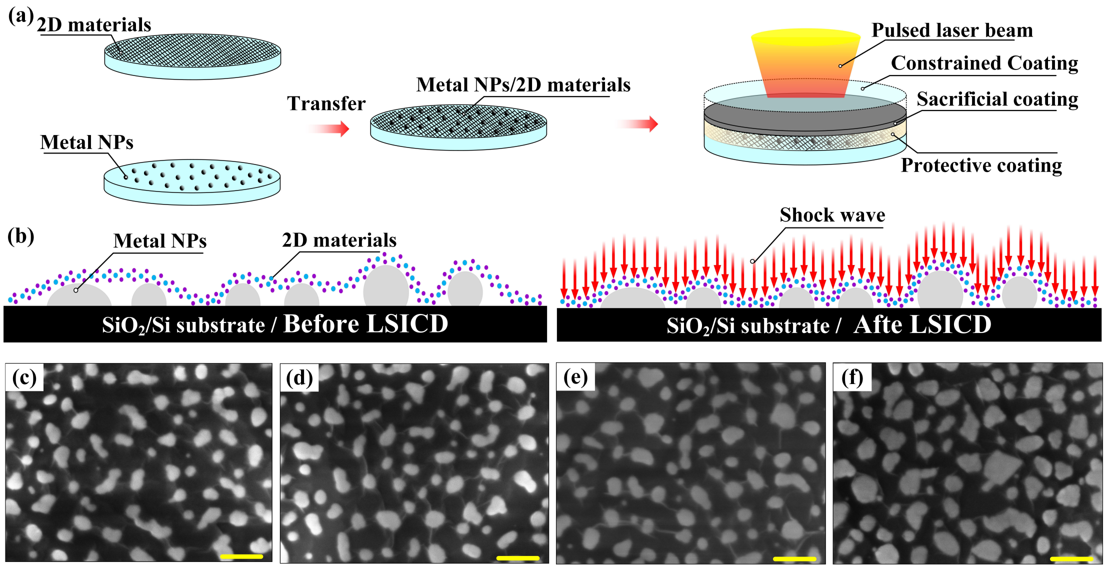

Fig. 1 (a) Schematic laser shock of metal nanoparticles/MoS$_2$ composite structure. (b) Schematic diagram of morphology of metal nanoparticles/MoS$_2$ composite structure before and after LSICD. (c-f) Scanning electron microscope (SEM) image of metal nanoparticles/MoS$_2$ composite structure before (c) and after (d-f) LSICD. Scale bar: 200 nm.

The mechanical properties of the material matter. We simulated the morphological changes of 2D materials suspended on rigid nanoparticles and different metal nanoparticles under laser shock by MD, as shown in Fig. 2. It can be seen that the Si NPs and Ti NPs were almost not deformed during the laser shock process, and as the 2D materials was impacted on hard NPs, the films on the top of nanoparticles was subjected to enormous stress, resulting in cracks. With the continuous movement of Al plate, the crack will further expand, and this large-area crack would greatly affect the mechanical and photoelectric properties of the 2D materials. Metal nanoparticles with lower yield strengths, such as Au, Ag and Al, could introduce cooperative deformation with 2D materials under laser shock, reducing the generation of defects.

MD simulations of the whole surface and strain distributions are shown in Fig. S2. As the Al plate moves downward, the metal nanoparticles gradually deform, and MoS$_2$ films approaches the substrate and wraps the nanoparticles (Fig. S2a(Ⅰ-Ⅱ)). When the Al plate collides with the substrates and rebounds, the gap between MoS$_2$ films and the substrate becomes larger due to the interaction between Al plate and MoS$_2$ and the stress waves propagating along the plane (larger than reality due to total reflection at the flat surface in the simulation) after MoS$_2$ films collided with the substrate at high speed (Fig. S2a(Ⅲ)). Then, after the Al plate leaves, the stress waves propagating along the plane will continue to adjust the gap between MoS$_2$ films and the substrate. With the gradual dissipation of the energy of the stress wave, the nanoparticles were finally wrapped under the interaction between the nanoparticles, the substrate and the film (Fig. S2a(Ⅳ)).

Fig. 2 Atomic snapshots of different NPs/MoS_2 deformation under LSICD at the same impact velocity. (a) Si NP/MoS_2. (b) Ag NP/MoS_2. (c) Au NP/MoS_2. (d) Al NP/MoS_2. (e) Ti NP/MoS_2.

Schematic diagram of the deformation was depicted in Fig. 3(a). When the monolayer MoS_2 films were transferred on top of nanoparticles, they were supported like a tent, and MoS_2 were bonded to it only on the top of the nanoparticles. Wrinkles were relaxed at this stage. Under the action of laser shock pressure, MoS_2 quickly attached to the flat plane, leaving no time for relaxation transferred from other areas. After the impact, the vdW force between MoS_2 and nanoparticles can maintain this state, and the contact area between the three-dimensional surface of nanoparticles and MoS_2 becomes larger, so as to achieve greater strain (Fig. 3(b)). This was also confirmed by SEM images of NPs/MoS_2 structure before and after LSICD (Fig. 3(d-e)). The maximum atomic strain of monolayer MoS_2 after LSICD was 10%. In the process of MoS_2 films approaching the substrate, the strain region of the films increased and the strain energy increased sharply. When the films contacted the substrates, the maximum atomic strain appeared at the top of the nanoparticles and gradually decreased from the center along both sides, while there was basically no strain in the flat area in full contact with the substrates.

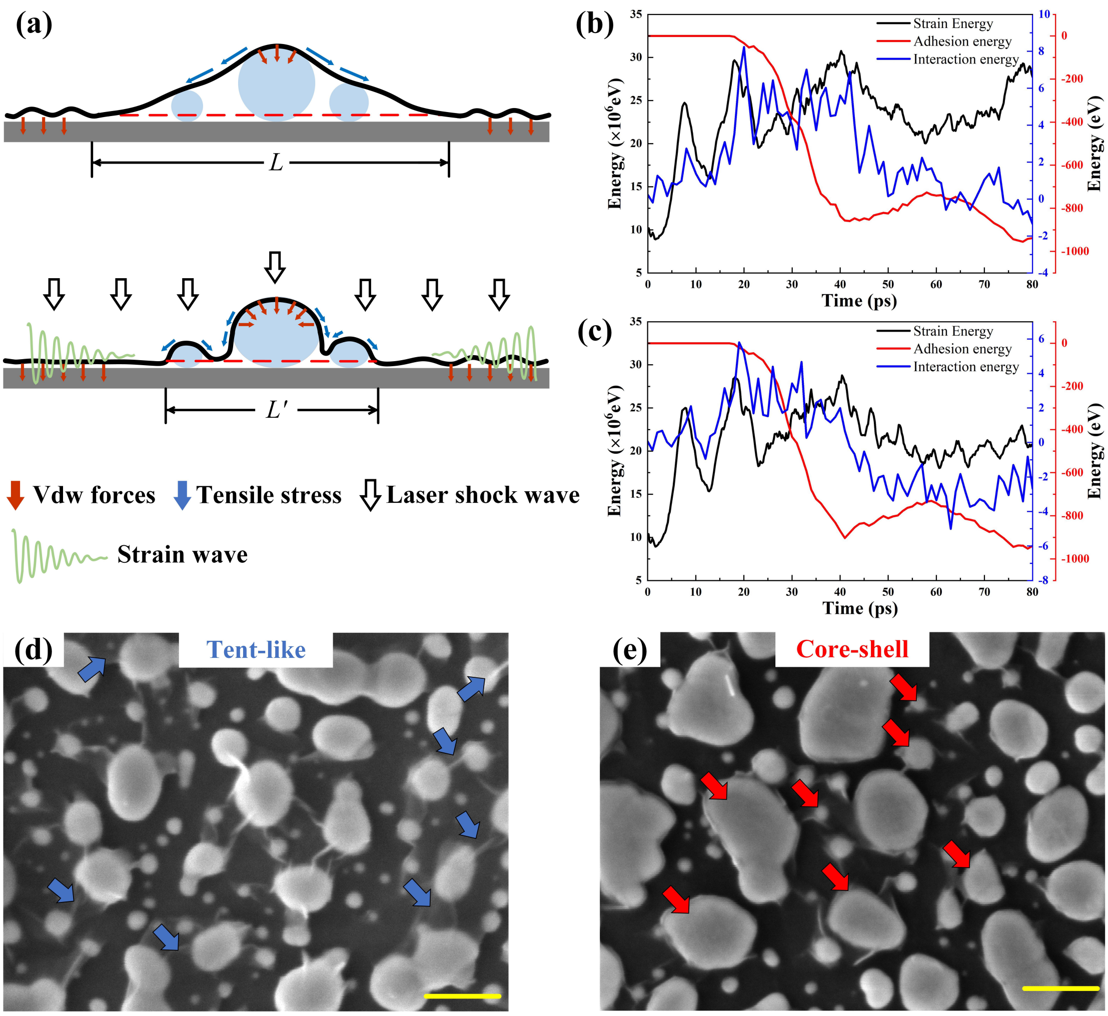

Fig. 3 (a) Schematic diagram of atomic force distribution (vdW force and tensile stress between the layers) for half-profile of MoS_2 during LSICD. Time evolution of adhesion energy, strain energy and interaction energy of Ag NPs/MoS_2 (b) and Au NPs/MoS_2 (c). (d-e) SEM images of metal NPs and MoS_2 before and after LSICD. Scale bar: 200 nm.

Tensile strain leads to the softening of lattice spring constant, which in turn influences crystal phonon modes. Raman spectroscopy is used to study the phonon modes, identify and characterize the strain on MoS_2 before and after laser shock. As shown in Fig. 4, the Raman spectrum of MoS_2 has two obvious characteristic vibration modes, E^1_{2g} at 385.4 cm^{-1} and A_{1g} at 405.8 cm^{-1}, which correspond to the in-plane vibration mode and out of plane vibration mode respectively. After the monolayer MoS_2 was transferred to the M@MO NPs substrates, the E^1_{2g} red shifted by 0.6 cm^{-1} relative to the as-grown MoS_2. After shock treatment with different laser energy, the E^1_{2g} first red shifted and then blue shifted, with a maximum red shift of 3.3 cm^{-1}. The E^1_{2g} was proven as highly sensitive relative to the uniaxial tensile strain because strain induced crystal symmetry breaking in the TMDs softened the double degenerate in-plane vibration[36–38]. Thus, the change of E^1_{2g} shows that MoS_2 produces strain when transferred to M@MO NPs substrates, and the strain increases after LSICD. Compared with previous literature reports[39], M@MO NPs/MoS_2 produces about 0.2% tensile strain, and the averaged maximum strain of MoS_2 was about 1.2% after laser shock.

Fig. 4 (a) Raman and (b) photoluminescence spectra of monolayer MoS_2 and M@MO NPs/MoS_2 before and after LSICD. (c) The frequencies of E^1_{2g} and A_{1g} modes extracted from (a) and the PL peaks of MoS_2 films on M@MO NPs extracted from (b).

The strain induced band gap reduction was consistent with the existing theoretical and experimental reports[36,38,40], which confirms the reduction of band gap and effectively transfers the strain to MoS_2 samples. The Raman and PL intensity of MoS_2 transferred to M@MO NPs was significantly enhanced (shown in Fig. S6), which is mainly due to the strong plasmonic effect of Ag nanoparticles, which amplifies the light field around the nanoparticles. We also note that the observed strain and plasmonic enhancement factors are the average of the ≈ 1 μm sample region (limited by the size of the laser spot), while the highest strain and plasmonic enhancement could be much larger.

The monolayer MoS_2 FETs and MoS_2 FETs transferred to M@MO NPs (NPs/MoS_2 FETs) were fabricated to investigate the effect of strain on the electrical properties of MoS_2 films. In this paper, our prefabricated metal electrode was mechanically laminated and transferred on M@MO NPs/MoS_2, so as to retain the lattice and inherent properties of 2D materials[41–45]. Fig. 5 showed the transfer characteristic curves and output characteristic curves of MoS_2 FETs, NPs/MoS_2 FETs and M@MO NPs/MoS_2 FETs after LSICD (LSICD NPs/MoS_2 FETs). As can be seen from Fig. 5c, the output current of MoS_2 FETs was 3.8 μA, showing nonlinear *I-V* characteristics and schottky contact behavior. MoS_2 transferred to M@MO NPs shown linear behavior, which was ohmic contact behavior at room temperature. The change in the contact type between MoS_2 and the metal electrode may be related to the strain of the films. Recent studies have shown that tensile strain can reduce the contact energy barrier between MoS_2 and Au[46]. The maximum output currents of NPs/MoS_2 FETs and LSICD1 NPs/MoS_2 FETs were 96 μA and 134 μA, which was about 25 times and 35 times higher than that of MoS_2 FETs, respectively. When MoS_2 was transferred to M@MO NPs, the contact between electrode and MoS_2 changes from Schottky contact to ohmic contact, which can be attributed to the reduction of contact barrier caused by strain.

Fig. 5 (a) Output and (b) transfer characteristic curves of four types MoS_2 FETs under different bias voltages. (c) output and (d) transfer characteristic curve of MoS_2 FETs extracted from (a) and (b). The bias voltage is 16 V and 2.5 V, respectively.

Fig. 5d showed the transfer characteristic curves of MoS_2 FETs and NPs/MoS_2 FETs with or without LSICD under the source drain bias voltage of 2.5V, the open state current density of MoS_2 FETs was 0.07 μA/μm. Similar to the improvement of the output performance of NPs/MoS_2 FETs, the open state current density of NPs/MoS_2 FETs increased to 1.89 μA/μm, which was more than one order of magnitude higher than that of MoS_2 FETs. It was exciting that the On-state current density of the laser treated sample (LSICD1 NPs/MoS_2 FETs) reaches 2.73 µA/µm, which was 1.4 times higher than that of the sample without laser shock treatment. To further compare the electrical characteristics of devices, we calculated the device field-effect mobility (μ_{FE}) using the following equation

In this equation, is the maximum slope value in the transfer characteristic curve, L (20 um)/W (80 um) represents the channel aspect ratio of the device, C_{ox} is the capacitance value of 300nm silica gate oxide[47]. We calculated that the field effect mobility of MoS_2 FETs was 1.9 $cm^2V^{-1}s^{-1}$, and that of NPs/MoS_2 FETs was 36.1 $cm^2V^{-1}s^{-1}$. After MoS_2 was transferred to M@MO NPs, the mobility increased by nearly 20 times, and the μ_{FE} of LSICD1 NPs/MoS_2 FETs further increases (44.1 $cm^2V^{-1}s^{-1}$). As far as we know, this is the highest μ_{FE} value of the transistor made of MoS_2 synthesized by CVD with SiO_2 as gate material. We also calculated the carrier concentration and resistivity of MoS_2.

where V_{th} is the threshold voltage of the device, $V_G = 16$ V and e is the electronic charge. The carrier concentration of monolayer MoS_2 and Ag NPs/MoS_2 was 3.22×10^{12} cm^{-2} and 3.69×10^{12} cm^{-2}, respectively. After laser shock treatment, the carrier concentration of the sample was 3.93×10^{12} cm^{-2}. Although the μ_{FE} and carrier concentration decreased slightly for samples (LSICD3 NPs/MoS_2) treated with higher energy laser shock, their values were still higher in general than those directly transferred, and the carrier concentrations of the four types of samples were in the same order of magnitude.

Density functional theory (DFT) calculations have also been performed using the Vienna ab initio simulation package to reveal the increase in mobility of MoS_2 FETs caused by LSICD. Fig. S14 showed the band structure of MoS_2 under biaxial tensile strain of 1-3% and different bending heights. The bending heights are defined in the Supporting Information (SI) and the corresponding structures are shown in Fig. S15. The band gap of MoS_2 decreased both under biaxial strain and strain caused by bending, which corresponded to the red shift of PL spectrum. In order to estimate the change of carrier mobility of MoS_2, we calculated their effective masses. It could be acquired by fitting by the equation[48] . We performed quadratic fitting near the valence band maximum (VBM) and the conduction band minimum (CBM), then calculated the hole and electron effective mass of MoS_2 in both stretched and bended cases, as shown in Fig. S15. Under 3% biaxial strain and bending height of 4.96 Å, the electron effective mass of MoS_2 was 0.41 m_0 and 0.42 m_0 respectively, which were less than 0.48 m_0 in the strain free state, agreeing with the measurement results of FETs.

In summary, this paper proposes a strategy to modulate the strain by using the cooperative deformation of 2D materials and metal nanoparticles induced by laser shock. When 2D materials are transferred to M@MO NPs and deformed by laser shock, the ultra-high strain rate deformation of 2D materials and metal nanoparticles avoids the generation of film defects and cracks, and elastic strains build up. MoS_2 as typical 2D materials was used to verify the effectiveness of this method. Raman and PL spectra confirmed the increase in MoS_2 tensile strain and decrease in the bandgap after LSICD. Due to the reduction in the effective mass of electrons caused by strain, the field-effect mobility of the transistor increases to 44.1 $cm^2V^{-1}s^{-1}$, which is 23 times that of the MoS_2 FETs. This is the maximum value of MoS_2 FETs grown by CVD with SiO_2 as dielectric. As clean processing method, Laser shock will not unintentionally dope MoS_2. This pollution-free, large-scale and ultra-fast opto-mechanical nanomanufacturing method provides a general strategy for large-scale adjustment of 2D material strain, and is compatible with traditional semiconductor manufacturing. This would help advance the fabrication of two-dimensional nanoelectronic devices, and offer a significant boost for the wider application of two-dimensional materials in semiconducting devices.

Acknowledgments

This work was supported by the National Natural Science Foundation of China (Grant No. 51901162). The authors thank the support of the National Talent Program of China.

References

(1) Mohta, N.; Thompson, S. E. Mobility Enhancement. *IEEE Circuits Devices Mag.* **2005**, *21* (5), 18–23. https://doi.org/10.1109/MCD.2005.1517386.

(2) Cao, J.; Ertekin, E.; Srinivasan, V.; Fan, W.; Huang, S.; Zheng, H.; Yim, J. W. L.; Khanal, D. R.; Ogletree, D. F.; Grossman, J. C.; Wu, J. Strain Engineering and One-Dimensional Organization of Metal–Insulator Domains in Single-Crystal Vanadium Dioxide Beams. *Nat. Nanotechnol.* **2009**, *4* (11), 732–737. https://doi.org/10.1038/nnano.2009.266.

(3) Guinea, F.; Katsnelson, M. I.; Geim, A. K. Energy Gaps and a Zero-Field Quantum Hall Effect in Graphene by Strain Engineering. *Nat. Phys.* **2010**, *6* (1), 30–33. https://doi.org/10.1038/nphys1420.

(4) Smith, A. M.; Nie, S. Semiconductor Nanocrystals: Structure, Properties, and Band Gap Engineering. *Acc. Chem. Res.* **2010**, *43* (2), 190–200. https://doi.org/10.1021/ar9001069.

(5) Changgu, L.; Xiaoding, W.; W., K. J.; James, H. Measurement of the Elastic Properties and Intrinsic Strength of Monolayer Graphene. *Science (80-.).* **2008**, *321* (5887), 385–388. https://doi.org/10.1126/science.1157996.

(6) Akinwande, D.; Brennan, C. J.; Bunch, J. S.; Egberts, P.; Felts, J. R.; Gao, H.; Huang, R.; Kim, J. S.; Li, T.; Li, Y.; Liechti, K. M.; Lu, N.; Park, H. S.; Reed, E. J.; Wang, P.; Yakobson, B. I.; Zhang, T.; Zhang, Y. W.; Zhou, Y.; Zhu, Y. A Review on Mechanics and Mechanical Properties of 2D Materials—Graphene and Beyond. *Extrem. Mech. Lett.* **2017**, *13*, 42–77. https://doi.org/10.1016/j.eml.2017.01.008.

(7) Wu, W.; Wang, J.; Ercius, P.; Wright, N. C.; Leppert-Simenauer, D. M.; Burke, R. A.; Dubey, M.; Dogare, A. M.; Pettes, M. T. Giant Mechano-Optoelectronic Effect in an Atomically Thin Semiconductor. *Nano Lett.* **2018**, *18* (4), 2351–2357. https://doi.org/10.1021/acs.nanolett.7b05229.

(8) Castellanos-Gomez, A.; Roldán, R.; Cappelluti, E.; Buscema, M.; Guinea, F.; Van Der Zant, H. S. J.; Steele, G. A. Local Strain Engineering in Atomically Thin MoS2. *Nano Lett.* **2013**, *13* (11), 5361–5366. https://doi.org/10.1021/nl402875m.

(9) Shen, T.; Penumatcha, A. V.; Appenzeller, J. Strain Engineering for Transition Metal Dichalcogenides Based Field Effect Transistors. *ACS Nano* **2016**, *10* (4), 4712–4718. https://doi.org/10.1021/acsnano.6b01149.

(10) Christopher, J. W.; Vutukuru, M.; Lloyd, D.; Bunch, J. S.; Goldberg, B. B.; Bishop, D. J.; Swan, A. K. Monolayer MoS2 Strained to 1.3% With a Microelectromechanical System. *J. MICROELECTROMECHANICAL Syst.* **2019**, *28* (2), 254–263. https://doi.org/10.1109/JMEMS.2018.2877983.

(11) Goldsche, M.; Sonntag, J.; Khodkov, T.; Verbiest, G. J.; Reichardt, S.; Neumann, C.; Ouaj, T.; von den Driesch, N.; Buca, D.; Stampfer, C. Tailoring Mechanically Tunable Strain Fields in Graphene. *Nano Lett.* **2018**, *18* (3), 1707–1713. https://doi.org/10.1021/acs.nanolett.7b04774.

(12) Pérez Garza, H. H.; Kievit, E. W.; Schneider, G. F.; Staufer, U. Controlled,

Reversible, and Nondestructive Generation of Uniaxial Extreme Strains (>10%) in Graphene. *Nano Lett.* **2014**, *14* (7), 4107–4113. https://doi.org/10.1021/nl5016848.

(13) Zeng, M.; Liu, J.; Zhou, L.; Mendes, R. G.; Dong, Y.; Zhang, M. Y.; Cui, Z. H.; Cai, Z.; Zhang, Z.; Zhu, D.; Yang, T.; Li, X.; Wang, J.; Zhao, L.; Chen, G.; Jiang, H.; Rümmeli, M. H.; Zhou, H.; Fu, L. Bandgap Tuning of Two-Dimensional Materials by Sphere Diameter Engineering. *Nat. Mater.* **2020**, *19* (5), 528–533. https://doi.org/10.1038/s41563-020-0622-y.

(14) Shi, J.; Ma, D.; Han, G.-F.; Zhang, Y.; Ji, Q.; Gao, T.; Sun, J.; Song, X.; Li, C.; Zhang, Y.; Lang, X.-Y.; Zhang, Y.; Liu, Z. Controllable Growth and Transfer of Monolayer MoS2 on Au Foils and Its Potential Application in Hydrogen Evolution Reaction. *ACS Nano* **2014**, *8* (10), 10196–10204. https://doi.org/10.1021/nn503211t.

(15) Rice, C.; Young, R. J.; Zan, R.; Bangert, U.; Wolverson, D.; Georgiou, T.; Jalil, R.; Novoselov, K. S. Raman-Scattering Measurements and First-Principles Calculations of Strain-Induced Phonon Shifts in Monolayer MoS2. *Phys. Rev. B* **2013**, *87* (8). https://doi.org/10.1103/PhysRevB.87.081307.

(16) Castellanos-Gomez, A.; Roldan, R.; Cappelluti, E.; Buscema, M.; Guinea, F.; van der Zant, H. S. J.; Steele, G. A. Local Strain Engineering in Atomically Thin MoS2. *NANO Lett.* **2013**, *13* (11), 5361–5366. https://doi.org/10.1021/nl402875m.

(17) Zhang, Z.; Li, T. Determining Graphene Adhesion via Substrate-Regulated Morphology of Graphene. *J. Appl. Phys.* **2011**, *110* (8), 83526. https://doi.org/10.1063/1.3656720.

(18) Choi, J.; Kim, H. J.; Wang, M. C.; Leem, J.; King, W. P.; Nam, S. Three-Dimensional Integration of Graphene via Swelling, Shrinking, and Adaptation. *Nano Lett.* **2015**, *15* (7), 4525–4531.

(19) Li, H.; Contryman, A. W.; Qian, X.; Ardakani, S. M.; Gong, Y.; Wang, X.; Weisse, J. M.; Lee, C. H.; Zhao, J.; Ajayan, P. M.; Li, J.; Manoharan, H. C.; Zheng, X. Optoelectronic Crystal of Artificial Atoms in Strain-Textured Molybdenum Disulphide. *Nat. Commun.* **2015**, *6* (May). https://doi.org/10.1038/ncomms8381.

(20) Chen, W.; Gui, X.; Liang, B.; Liu, M.; Lin, Z.; Zhu, Y.; Tang, Z. Controllable Fabrication of Large-Area Wrinkled Graphene on a Solution Surface. *ACS Appl. Mater. Interfaces* **2016**, *8* (17), 10977–10984. https://doi.org/10.1021/acsami.6b00137.

(21) Kim, H.; Jang, Y. R.; Yoo, J.; Seo, Y.-S.; Kim, K.-Y.; Lee, J.-S.; Park, S.-D.; Kim, C.-J.; Koo, J. Morphology Control of Surfactant-Assisted Graphene Oxide Films at the Liquid–Gas Interface. *Langmuir* **2014**, *30* (8), 2170–2177. https://doi.org/10.1021/la403255q.

(22) Deng, S.; Che, S.; Debbarma, R.; Berry, V. Strain in a Single Wrinkle on an MoS 2 Flake for In-Plane Realignment of Band Structure for Enhanced Photo-Response. *Nanoscale* **2019**, *11* (2), 504–511.

(23) Liu, T.; Liu, S.; Tu, K. H.; Schmidt, H.; Chu, L.; Xiang, D.; Martin, J.; Eda, G.; Ross, C. A.; Garaj, S. Crested Two-Dimensional Transistors. *Nat. Nanotechnol.* **2019**, *14* (3), 223–226. https://doi.org/10.1038/s41565-019-0361-x.

(24) Kim, D. W.; Lee, J.; Kim, S. J.; Jeon, S.; Jung, H.-T. The Effects of the Crystalline Orientation of Cu Domains on the Formation of Nanoripple Arrays in CVD-Grown Graphene on Cu. *J. Mater. Chem. C* **2013**, *1* (47), 7819–7824. https://doi.org/10.1039/C3TC31717J.

(25) Kim, S. J.; Kim, D. W.; Lim, J.; Cho, S. Y.; Kim, S. O.; Jung, H. T. Large-Area Buckled MoS2 Films on the Graphene Substrate. *ACS Appl. Mater. Interfaces* **2016**, *8* (21), 13512–13519. https://doi.org/10.1021/acsami.6b01828.

(26) Ahn, G. H.; Amani, M.; Rasool, H.; Lien, D. H.; Mastandrea, J. P.; Ager, J. W.; Dubey, M.; Chrzan, D. C.; Minor, A. M.; Javey, A. Strain-Engineered Growth of Two-Dimensional Materials. *Nat. Commun.* **2017**, *8* (1), 1–7. https://doi.org/10.1038/s41467-017-00516-5.

(27) A., S. D.; Zhaohe, D.; Peng, W.; Arturo, C.-C.; J., B. C.; Rui, H.; Nanshu, L.

Mechanics of Spontaneously Formed Nanoblisters Trapped by Transferred 2D Crystals. *Proc. Natl. Acad. Sci.* **2018**, *115* (31), 7884–7889. https://doi.org/10.1073/pnas.1801551115.

(28) Li, T.; Zhang, Z. Snap-Through Instability of Graphene on Substrates. *Nanoscale Res. Lett.* **2009**, *5* (1), 169. https://doi.org/10.1007/s11671-009-9460-1.

(29) Hu, Y.; Li, J.; Tian, J.; Xuan, Y.; Deng, B.; McNear, K. L.; Lim, D. G.; Chen, Y.; Yang, C.; Cheng, G. J. Parallel Nanoshaping of Brittle Semiconductor Nanowires for Strained Electronics. *Nano Lett.* **2016**, *16* (12), 7536–7544. https://doi.org/10.1021/acs.nanolett.6b03366.

(30) Motlag, M.; Hu, Y.; Tong, L.; Huang, X.; Ye, L.; Cheng, G. J. Laser-Shock-Induced Nanoscale Kink-Bands in WSe2 2D Crystals. *ACS Nano* **2019**, *13* (9), 10587–10595. https://doi.org/10.1021/acsnano.9b04705.

(31) Motlag, M.; Kumar, P.; Hu, K. Y.; Jin, S.; Li, J.; Shao, J.; Yi, X.; Lin, Y.-H.; Walrath, J. C.; Tong, L.; Huang, X.; Goldman, R. S.; Ye, L.; Cheng, G. J. Asymmetric 3D Elastic–Plastic Strain-Modulated Electron Energy Structure in Monolayer Graphene by Laser Shocking. *Adv. Mater.* **2019**, *31* (19), 1900597. https://doi.org/https://doi.org/10.1002/adma.201900597.

(32) Hu, Y.; Zhang, F.; Titze, M.; Deng, B.; Li, H.; Cheng, G. J. Straining Effects in MoS2 Monolayer on Nanostructured Substrates: Temperature-Dependent Photoluminescence and Exciton Dynamics. *Nanoscale* **2018**, *10* (12), 5717–5724. https://doi.org/10.1039/C8NR00332G.

(33) Huang, G.; Yaowu, H.; Yi, X.; Ji, L.; Yingling, Y.; V., M. R.; Chunyu, L.; Jian, L.; Minghao, Q.; J., C. G. Large-Scale Nanoshaping of Ultrasmooth 3D Crystalline Metallic Structures. *Science (80-.).* **2014**, *346* (6215), 1352–1356. https://doi.org/10.1126/science.1260139.

(34) Wang, Y.; Jin, S.; Wang, Q.; Wu, M.; Yao, S.; Liao, P.; Kim, M. J.; Cheng, G. J.; Wu, W. Parallel Nanoimprint Forming of One-Dimensional Chiral Semiconductor for Strain-Engineered Optical Properties. *Nano-Micro Lett.* **2020**, *12* (1), 160. https://doi.org/10.1007/s40820-020-00493-3.

(35) Fairand, B. P.; Clauer, A. H. Laser Generation of High-amplitude Stress Waves in Materials. *J. Appl. Phys.* **1979**, *50* (3), 1497–1502. https://doi.org/10.1063/1.326137.

(36) Conley, H. J.; Wang, B.; Ziegler, J. I.; Haglund, R. F.; Pantelides, S. T.; Bolotin, K. I. Bandgap Engineering of Strained Monolayer and Bilayer MoS2. *Nano Lett.* **2013**, *13* (8), 3626–3630. https://doi.org/10.1021/nl4014748.

(37) Desai, S. B.; Seol, G.; Kang, J. S.; Fang, H.; Battaglia, C.; Kapadia, R.; Ager, J. W.; Guo, J.; Javey, A. Strain-Induced Indirect to Direct Bandgap Transition in Multilayer WSe 2. *Nano Lett.* **2014**, *14* (8), 4592–4597. https://doi.org/10.1021/nl501638a.

(38) He, K.; Poole, C.; Mak, K. F.; Shan, J. Experimental Demonstration of Continuous Electronic Structure Tuning via Strain in Atomically Thin MoS2. *Nano Lett.* **2013**, *13* (6), 2931–2936. https://doi.org/10.1021/nl4013166.

(39) John, A. P.; Thenapparambil, A.; Thalakulam, M. Strain-Engineering the Schottky Barrier and Electrical Transport on MoS2. *Nanotechnology* **2020**, *31* (27), 275703. https://doi.org/10.1088/1361-6528/ab83b7.

(40) Song, S.; Keum, D. H.; Cho, S.; Perello, D.; Kim, Y.; Lee, Y. H. Room Temperature Semiconductor-Metal Transition of MoTe2 Thin Films Engineered by Strain. *Nano Lett.* **2016**, *16* (1), 188–193. https://doi.org/10.1021/acs.nanolett.5b03481.

(41) Liu, L.; Kong, L.; Li, Q.; He, C.; Ren, L.; Tao, Q.; Yang, X.; Lin, J.; Zhao, B.; Li, Z.; Chen, Y.; Li, W.; Song, W.; Lu, Z.; Li, G.; Li, S.; Duan, X.; Pan, A.; Liao, L.; Liu, Y. Transferred van Der Waals Metal Electrodes for Sub-1-Nm MoS2 Vertical Transistors. *Nat. Electron.* **2021**, *4* (5), 342–347. https://doi.org/10.1038/s41928-021-00566-0.

(42) Wang, Y.; Kim, J. C.; Wu, R. J.; Martinez, J.; Song, X.; Yang, J.; Zhao, F.; Mkhoyan, K. A.; Jeong, H. Y.; Chhowalla, M. Van Der Waals Contacts between Three-Dimensional Metals and Two-Dimensional Semiconductors. *Nature*

2019, *568* (7750), 70-+. https://doi.org/10.1038/s41586-019-1052-3.

(43) Jung, Y.; Choi, M. S.; Nipane, A.; Borah, A.; Kim, B.; Zangiabadi, A.; Taniguchis, T.; Watanabe, K.; Yoo, W. J.; Hone, J.; Teherani, J. T. Transferred via Contacts as a Platform for Ideal Two-Dimensional Transistors. *Nat. Electron.* **2019**, *2* (5), 187–194. https://doi.org/10.1038/s41928-019-0245-y.

(44) Liu, Y.; Huang, Y.; Duan, X. Van Der Waals Integration before and beyond Two-Dimensional Materials. *Nature* **2019**, *567* (7748), 323–333. https://doi.org/10.1038/s41586-019-1013-x.

(45) Liu, Y.; Guo, J.; Zhu, E.; Liao, L.; Lee, S.-J.; Ding, M.; Shakir, I.; Gambin, V.; Huang, Y.; Duan, X. Approaching the Schottky-Mott Limit in van Der Waals Metal-Semiconductor Junctions. *Nature* **2018**, *557* (7707), 696-+. https://doi.org/10.1038/s41586-018-0129-8.

(46) Pak, S.; Lee, J.; Jang, A.-R.; Kim, S.; Park, K.-H.; Sohn, J. I.; Cha, S. Strain-Engineering of Contact Energy Barriers and Photoresponse Behaviors in Monolayer MoS2 Flexible Devices. *Adv. Funct. Mater.* **2020**, *30* (43), 2002023. https://doi.org/https://doi.org/10.1002/adfm.202002023.

(47) Yu, Z.; Pan, Y.; Shen, Y.; Wang, Z.; Ong, Z.-Y.; Xu, T.; Xin, R.; Pan, L.; Wang, B.; Sun, L.; Wang, J.; Zhang, G.; Zhang, Y. W.; Shi, Y.; Wang, X. Towards Intrinsic Charge Transport in Monolayer Molybdenum Disulfide by Defect and Interface Engineering. *Nat. Commun.* **2014**, *5* (1), 5290. https://doi.org/10.1038/ncomms6290.

(48) Zhong, M.; Zeng, W.; Liu, F.-S.; Tang, B.; Liu, Q.-J. Optical Transparency, Carrier Mobility, and Electrical Conductivity of La-Based Copper Layered Oxychalcogenides: A Density Functional Theory Study. *Sol. Energy* **2020**, *204*, 346–353. https://doi.org/https://doi.org/10.1016/j.solener.2020.04.091.

Supporting Information

Large-scale ultra-fast strain engineering of CVD-grown two-dimensional materials on self-limited deformable nanostructures towards enhanced field effect transistors

Zheng Huang [a], Nan Lu [c], Zifeng Wang [a], Shuoheng Xu [a], Jie Guan [c], Yaowu Hu [a,b*]

[a] The Institute of Technological Sciences, Wuhan University, Wuhan, 430072, China

[b] School of Power and Mechanical Engineering, Wuhan University, Wuhan 430072, China

[c] School of Physics, Southeast University, Nanjing 211189, China

Simulation method

Molecular dynamics (MD) simulation

MD simulations were performed using the LAMMPS code[1]. In the simulation, it is assumed that metal nanoparticles and Al piston were face-centered cubic (FCC) single crystal structures. The lattice constants are 4.09 and 3.9860 Å, respectively. A shock wave was generated by applying an initial velocity to the Al piston. The diameter of metal nanoparticles was 5 nm. Mixed pair styles are used in calculations. The embedded atom method (EAM) potential is used to describe metal nanoparticles and Al piston. Stillinger Weber (SW) potential is used to describe the interaction between atoms in monolayer MoS_2. The interaction between Ag, Au, Cu, Si and MoS_2 was described by 12-6 Lennard Jones potential. MD simulation was carried out using a micro canonical ensemble (NVE) with a temperature of about 300 K, and the position of metal nanoparticles was fixed in the XY plane by fix recenter codes. The simulation time step is set to 1 fs. Ovito software is used for structure visualization.

Density Functional Calculations

The density functional theory (DFT) calculations were performed via the Vienna ab initio simulation package (VASP)[2]. Effective potential between ionic cores and electrons was described by the projector augmented wave (PAW) method[3]. We choose the generalized gradient approximation (GGA) in the Perdew-Burke-Ernzerhof (PBE) parametrization for the exchange-correlation functional[4]. Band structure was calculated along the symmetry points Γ, X, S, Y, Γ. The k-point sampling of the first Brillouin zone was done with a 2×8×1 Γ-centered k-points grid[5]. The energy cutoff was set to 500 eV for all cases. All the geometries were optimized using the conjugated-gradient method[6] until a Hellman-Feynman force convergence threshold of 10^{-3} eV/Å, with the energy differences are converged within 10^{-6} eV for each self-consistency iteration. To avoid the interactions between adjacent layers, the vacuum region is set in excess of 25 Å

Experimental Methods

Growth of monolayer MoS_2

Monolayer MoS_2 was grown in a BEQ double temperature zone tubular furnace by chemical vapor deposition, as shown in Fig. S3. The tube furnace was vacuumized to 1 Pa in advance and purged with 200 sccm Ar gas for 15 minutes to minimize O_2 content. The SiO_2/Si substrate was soaked in piranha solution for 2 hours, then cleaned with deionized water, acetone, absolute ethanol and deionized water for 10 minutes, and then dried with N_2. Spin the prepared Na_2MoO_4 solution (4 mg/ml) on the SiO_2/Si substrates, then put the SiO_2/Si substrates and 50 mg sulfur powders into the double temperature zone tubular furnace. The sulfur powders were located in the separate heating zone upstream. The area containing sulfur powders and Na_2MoO_4 was heated to 150 ℃and 800 ℃, respectively. After growing under the condition of Ar/H_2 gas flow rate of 60 sccm for 15 minutes, stop the process, and then increase the Ar/H_2 gas flow rate to 400 sccm to quickly cool the samples.

Fabrication of M@MO NPs and MoS_2 FETs

The Ag films were deposited on Si/SiO_2 (the thickness of SiO_2 was 300 nm) substrates by DC magnetron sputtering, and then the deposited Ag films were annealed in a tubular furnace at 200℃ for 30 min in an air environment to form M@MO NPs. The as-grown monolayer MoS_2 was transferred to Si/SiO_2 substrate with Ag NPs by polymethylmethacrylate (PMMA) assisted wet transfer method. The metal electrode of FETs was fabricated by UV exposure and thermal evaporation deposition, and the deposition thickness of Au electrodes were 100 nm. The Au electrodes deposited on Si/SiO_2 substrate were transferred to M@MO NPs/MoS_2 by PMMA assisted dry transfer method to complete the fabrication of FETs. The specific method was as follows: Firstly, spin coating PMMA on the surface of Au electrodes, heat it at 120℃ on the hot plate for 2 min, immerse PMMA/Au electrodes in 2 mol/L KOH solution for 30 min, separate it from Si/SiO_2 substrate, dilute it with deionized water for many times, and transfer it to MoS_2 using a home-made transfer platform. Then, heat the transferred samples on the hot plate at 60℃ for 30 min to improve the contact between the electrode and MoS_2. Finally, remove the residual PMMA with a large amount of acetone and isopropanol.

Laser shock treatment

The Nd: YAG laser (pulse width: 9 ns, wavelength: 1064 nm) was used as energy for laser shock treatment of M@MO NPs/MoS_2. In short, a 4 um Al foil sacrificial layer coated with graphite was covered on the surface of the prepared MoS_2 FETs to absorb laser energy. Under the irradiation of pulsed laser, the graphite layer evaporates and ionizes instantaneously, and the expanded plasma is limited by the transparent limiting layer, so an instantaneous pressure shock wave is generated. Here, Al foil was used as the momentum transfer layer to transfer the pressure shock wave to the metal electrode and induce the deformation of the metal electrode and MoS_2. The beam diameter (typically around 5 mm) was controlled by the focusing lens and calibrated with photosensitive paper.

Characterization

The morphology of M@MO NPs and MoS_2 were examined with scanning electron microscope (SEM, Tescan Mira3). The surface profile of the sample before and after laser shock was measured in touch mode using MicroNano D-5A atomic force microscope. Raman scattering spectrum and photoluminescence spectrum are obtained on Zolix RTS2 Micro confocal Raman spectral system. The laser light source was 532 nm laser. The Raman laser energy was kept low to avoid any heating effect. The MoS_2 and Ag NPs/MoS_2 FETs were tested in a vacuum probe station. The system was kept at $\sim 1\times10^{-2}$ Pa during the measurement. A Keithley 2636B System SourceMeter was used to carry out the electric measurement.

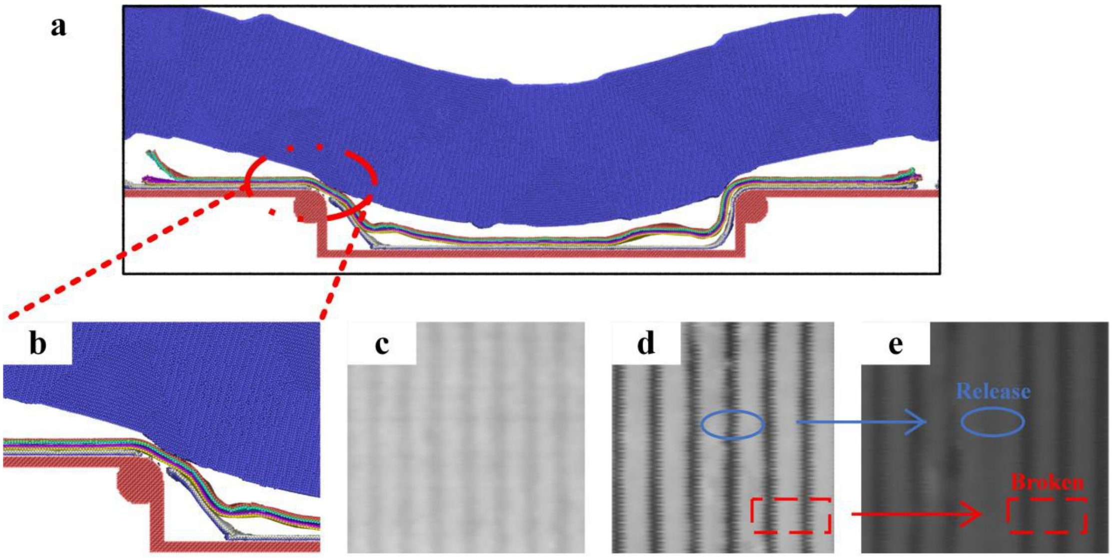

Fig. S1 (a) Atomic snapshot of the laser shock response of multilayered 2D materials spread on rigid template by MD calculations. (b) Detail diagram of fracture location of 2D materials after laser shock. SEM images of multilayer 2D materials spread on rigid template before (c) and after (d-e) laser shock. (e) SEM image after strain release.

From the SEM of the sample after laser impact, the black stripe is due to the 2D materials being pressed into the mold (Fig. S1(d)). However, the release of strain shows the breaken parts at the edge of the corners (Fig. S1(e)).

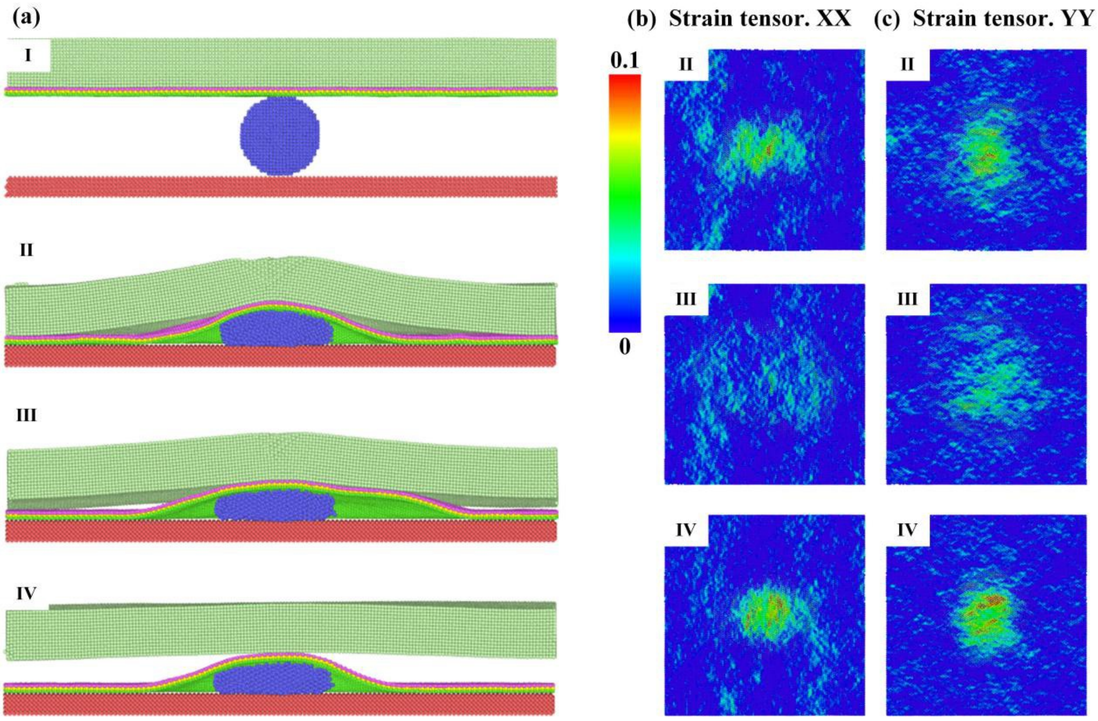

Fig. S2 (a) Atomic snapshots of Ag NPs/MoS_2 (cross section) during LSICD at different time steps (Ⅰ-Ⅳ:0ps, 40ps, 60ps and 80 ps). Impactor speed: 0.25 km/s. (b-c) Time evolution of strain tensor XX and strain tensor YY of MoS_2 (top view).

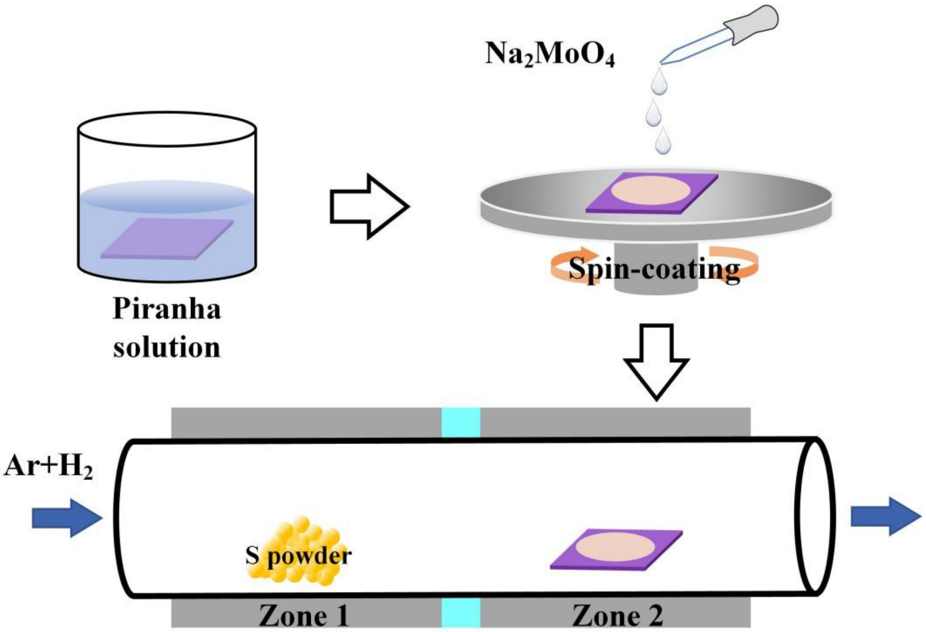

Fig. S3 Schematic illustration of monolayer MoS_2 films growth process.

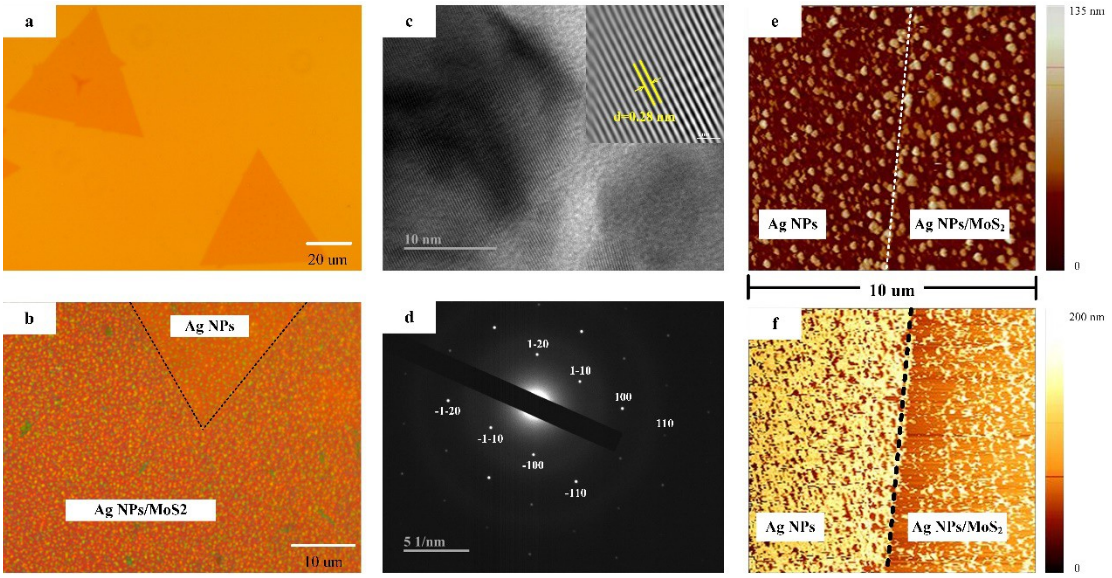

Fig. S4 (a) Optical image of monolayer MoS_2 films grown by chemical vapor deposition. (b) Optical image of monolayer MoS_2 films transferred to Ag Nanoparticles. (c) High-resolution TEM image of MoS_2 films. (d) SAED pattern of MoS_2 films. (e-f) AFM images of monolayer MoS_2 films transferred to Ag Nanoparticles.

The monolayer MoS_2 grown by CVD used in the experiment, as shown in Fig. S4(a), the side length of the triangle was about 60 um. HR-TEM images of MoS_2 showed the three interplanar distances were 0.27 nm. The optical and AFM images of M@MO NPs/MoS_2 were shown in Fig. S4(b, e-f). The rough substrate can be seen, and the area with or without MoS_2 can be clearly distinguished.

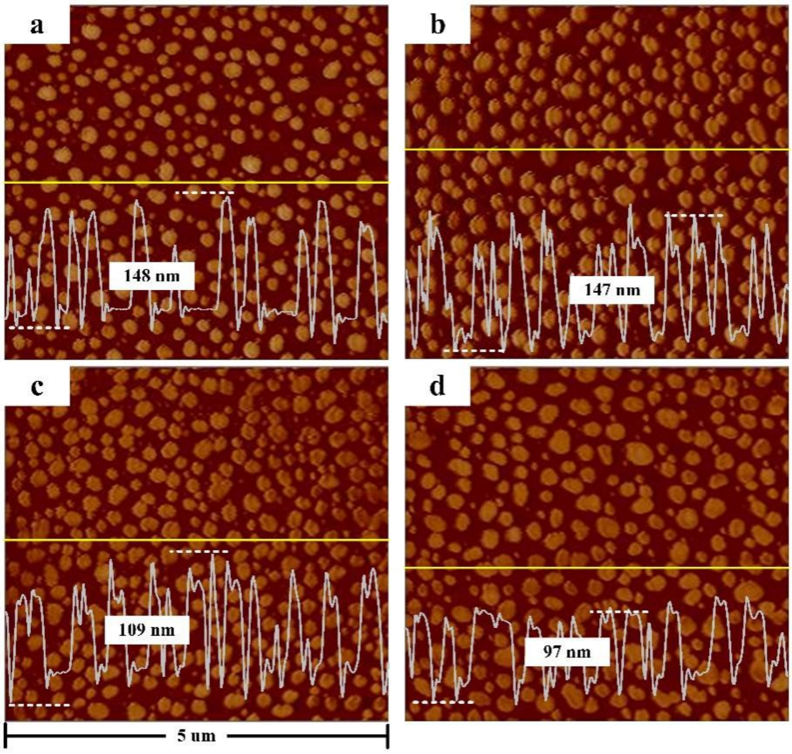

Fig. S5 (a) AFM images of Ag NPs/MoS$_2$ by transferring monolayer MoS$_2$ onto Ag nanoparticles formed by magnetron sputtering for 30s and annealing. (c-d) AFM images of Ag NPs/MoS$_2$ after LSICD.

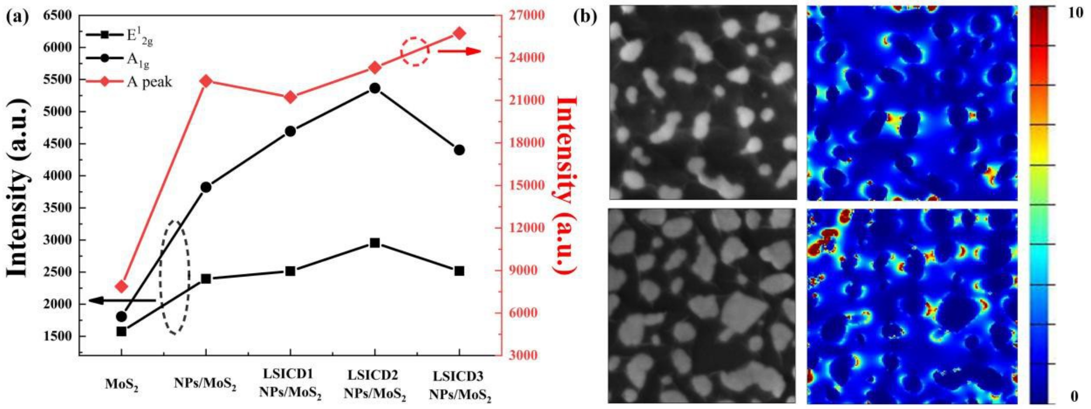

Fig. S6 (a) Intensities of characteristic peaks of Raman and PL spectra of MoS$_2$ under LSICD. (b) Distributions of the square of electric field ($|E|^2/|E_0|^2$) at NPs/MoS$_2$ before and after LSICD at 532 nm excitation (top view).

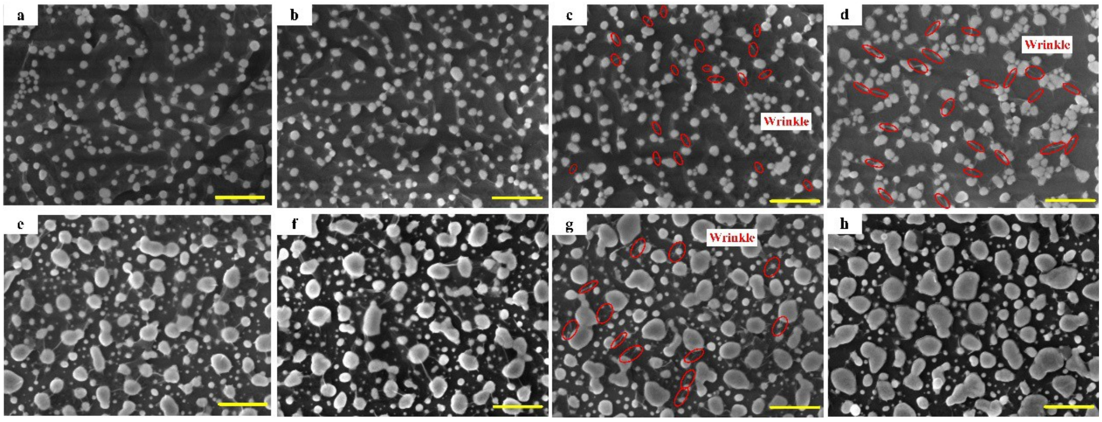

Fig. S7 (a) SEM images of Ag NPs/MoS_2 by transferring monolayer MoS_2 onto Ag nanoparticles formed by magnetron sputtering for 15s and annealing. (b-d) SEM images of Ag NPs/MoS_2 after LSICD. (e) SEM images of Ag NPs/MoS_2 by transferring monolayer MoS_2 onto Ag nanoparticles formed by magnetron sputtering for 45s and annealing. (f-h) SEM images of Ag NPs/MoS_2 after LSICD. Scale bar: 500 nm.

Fig. S7 shown SEM images of monolayer MoS_2 films on various sizes of Ag NPs and Ag NPs/MoS_2 structures by LSICD. The results indicated that the transferred monolayer MoS_2 films were supported by nanoparticles like tents. After laser shock, the nanoparticles were deformed due to the impact force. The MoS_2 films were bonded to the three-dimensional surface of nanoparticles to form a core-shell like structure.

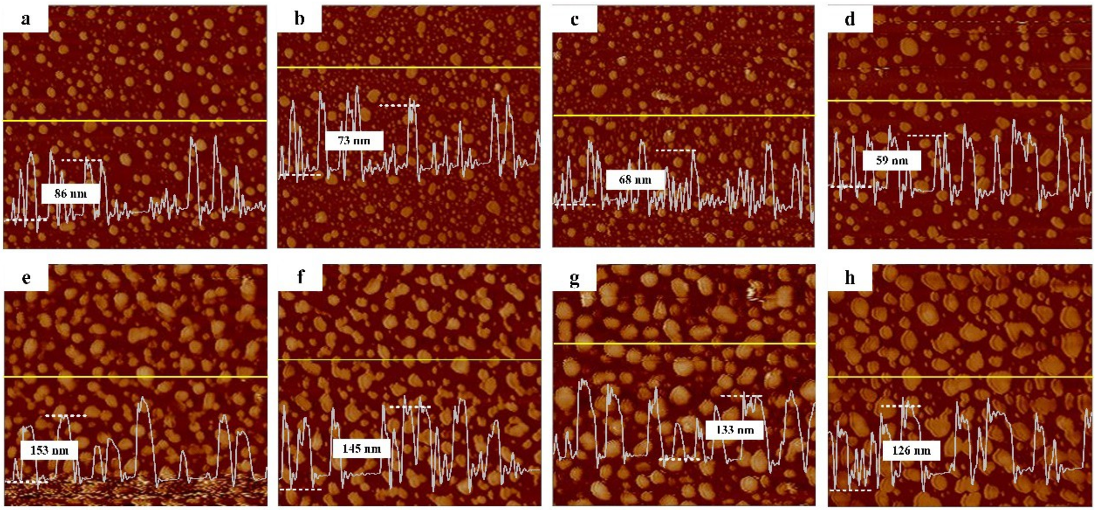

Fig. S8 (a) AFM images of Ag NPs/MoS_2 by transferring monolayer MoS_2 onto Ag nanoparticles formed by magnetron sputtering for 15s and annealing. (b-d) AFM images of Ag NPs/MoS_2 after LSICD. (e) AFM images of Ag NPs/MoS_2 by transferring monolayer MoS_2 onto Ag nanoparticles formed by magnetron sputtering for 45s and annealing. (f-h) AFM images of Ag NPs/MoS_2 after LSICD. Scale bar: 500 nm.

Fig. S8 shown the AFM diagram of monolayer MoS_2 films on various sizes of Ag NPs and Ag NPs/MoS_2 structures by LSICD. As a result, with the increase of laser shock energy, the nanoparticles had different degrees of deformation, the particle height became smaller, the transverse size increases, and the top became more flat.

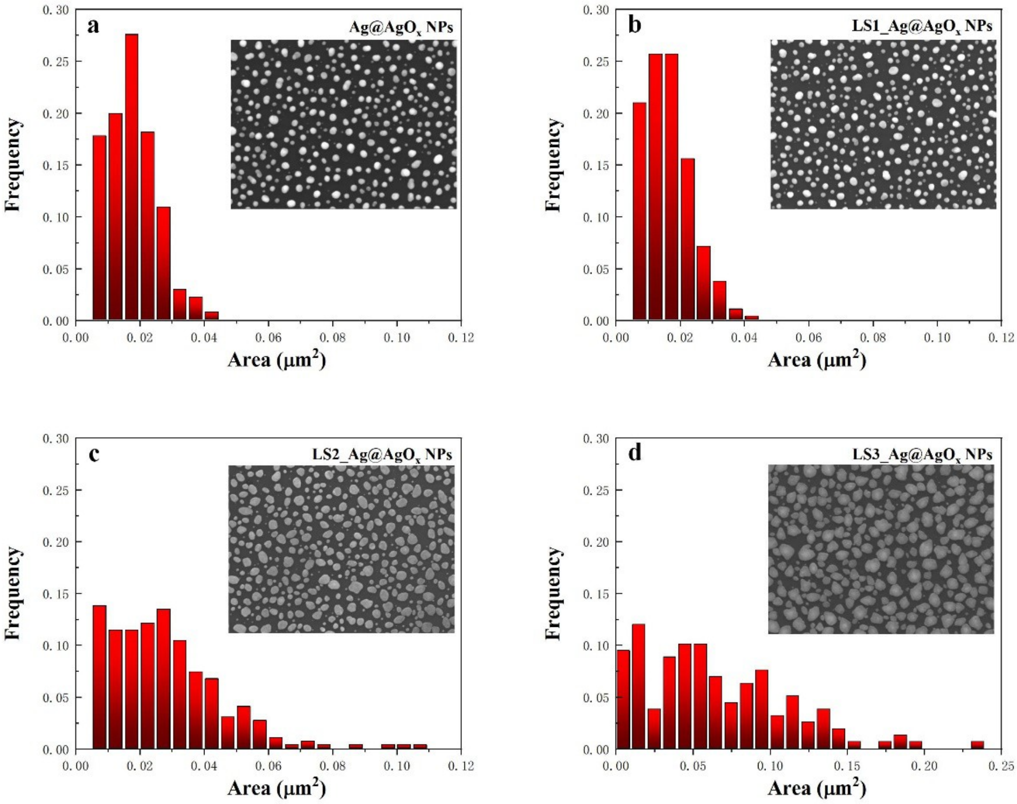

Fig. S9 (a) Statistical area distribution of Ag nanoparticles formed by magnetron sputtering for 30s and annealing. (b-d) Statistical area distribution of Ag nanoparticles after LSICD.

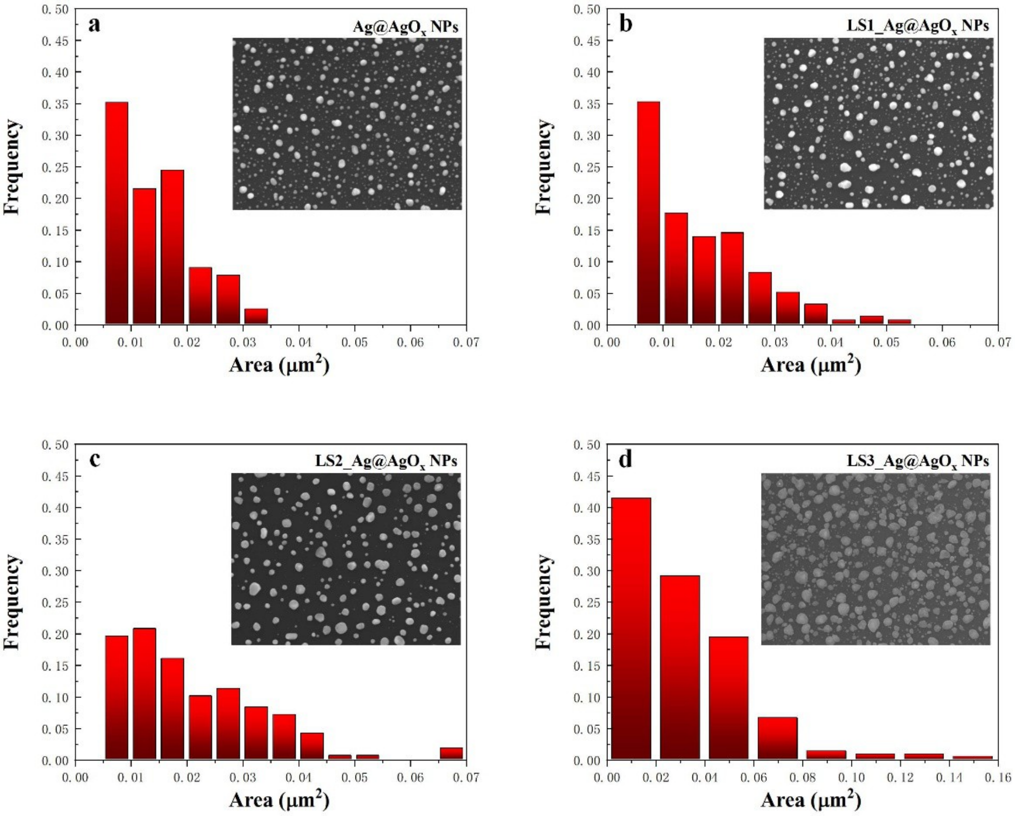

Fig. S10 (a) Statistical area distribution of Ag nanoparticles formed by magnetron sputtering for 15s and annealing. (b-d) Statistical area distribution of Ag nanoparticles after LSICD.

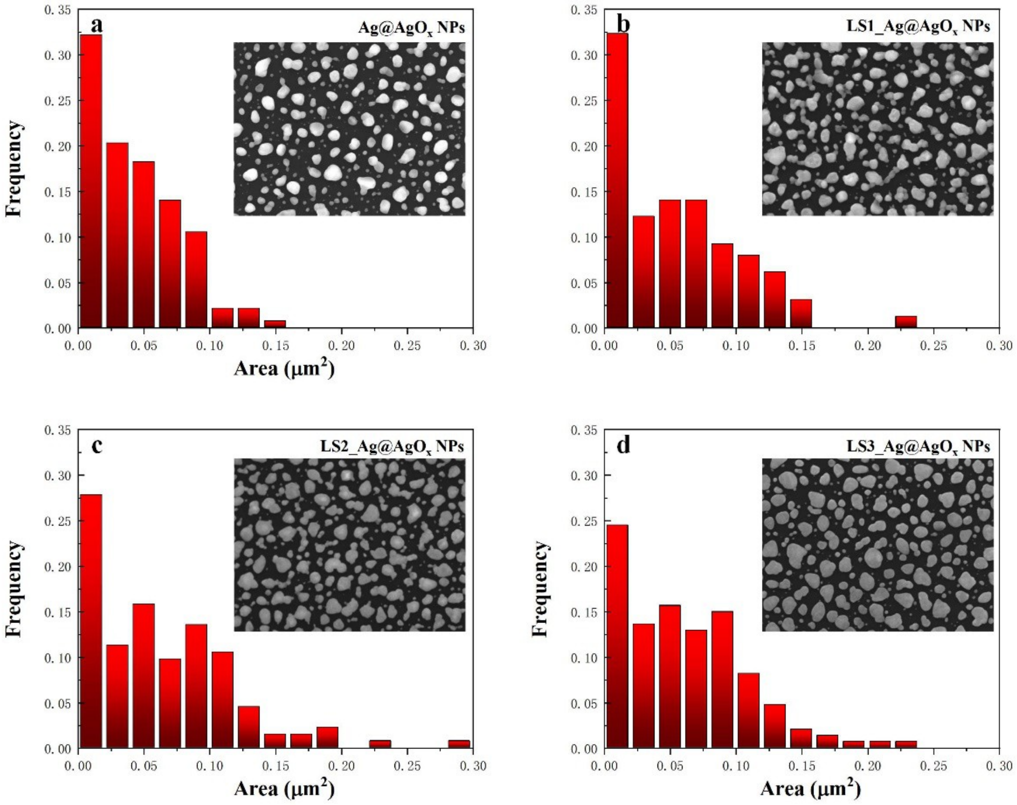

Fig. S11 (a) Statistical area distribution of Ag nanoparticles formed by magnetron sputtering for 45s and annealing. (b-d) Statistical area distribution of Ag nanoparticles after LSICD.

Fig. S9-11 shown the SEM diagram of Ag NPs with different sizes by LSICD. With the increase of laser shock energy, due to the flattening of nanoparticles, the area occupied by single nanoparticles increases and the gap between particles decreases. This was consistent with the AFM measurement.

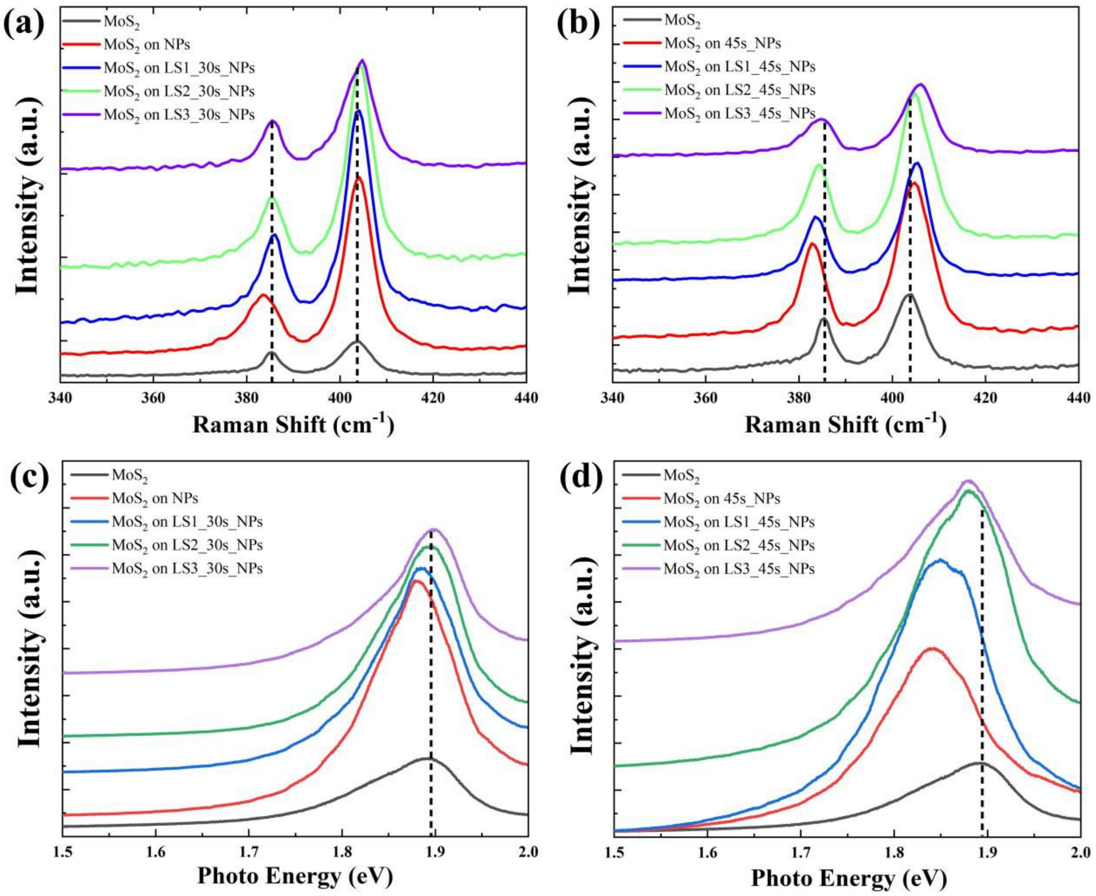

Fig. S12 (a) and (b) Raman spectra of monolayer MoS_2 films on different sizes nanoparticles by laser shock without and with the participation of MoS_2, respectively. (c) and (d) Photoluminescence (PL) spectra of monolayer MoS_2 films on different sizes nanoparticles by laser shock without and with the participation of MoS_2, respectively.

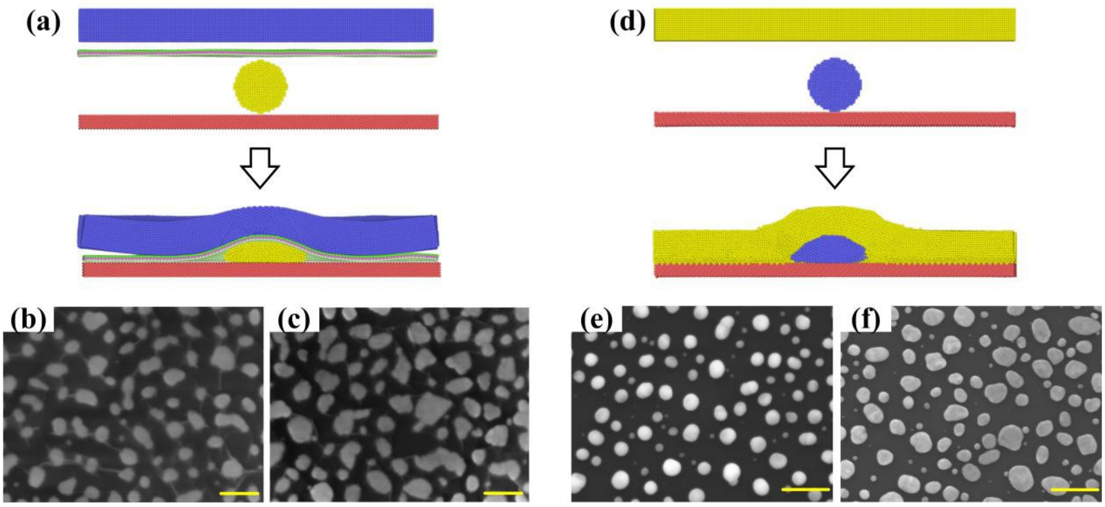

Fig. S13 (a) MD simulation results of Ag NPs/MoS_2 structure during LSW. (b-c) SEM images of Ag NPs/MoS_2 structure before and after LSICD. (d) MD simulation results of single Ag NPs during laser shock. (e-f) SEM images of Ag NPs/MoS_2 structure before and after laser shock. Scale bar: 200 nm.

We transferred the monolayer MoS_2 films to the deformed nanoparticles and tested their Raman and PL spectra, as shown in Fig. S12. As the deposition time increased, the size and height of nanoparticles increased, and the red shift of Raman and PL characteristic peak of MoS_2 on nanoparticles also increased. Fig. S13 showed the deformation responses of individual nanoparticles with and without MoS_2 structures. The deformation in NPs/MoS_2 structures were larger and with smaller surface curvature than that of single nanoparticles during laser shock. This resulted in much less strain levels if the laser shock was carried out without the participation of MoS_2.

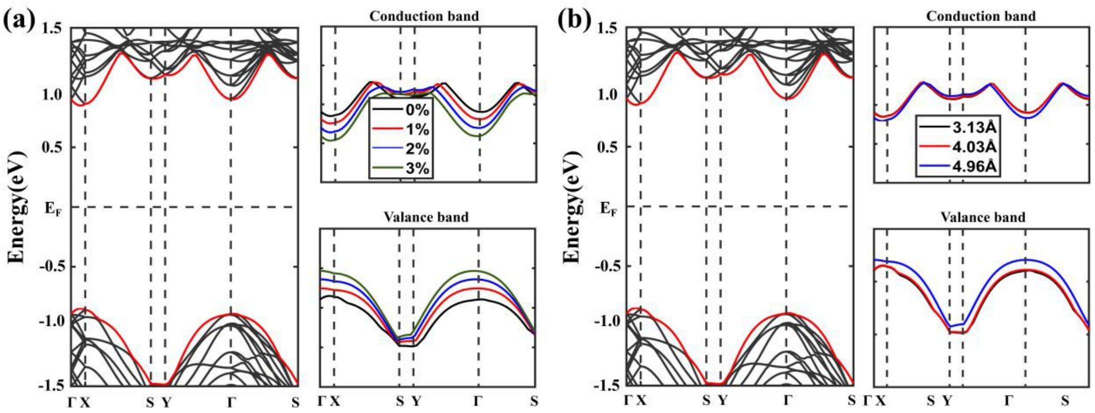

Fig. S14 (a) Band structure of monolayer MoS_2 with different biaxial tensile strain. (b) Band structure of monolayer MoS_2 with different bending heights.

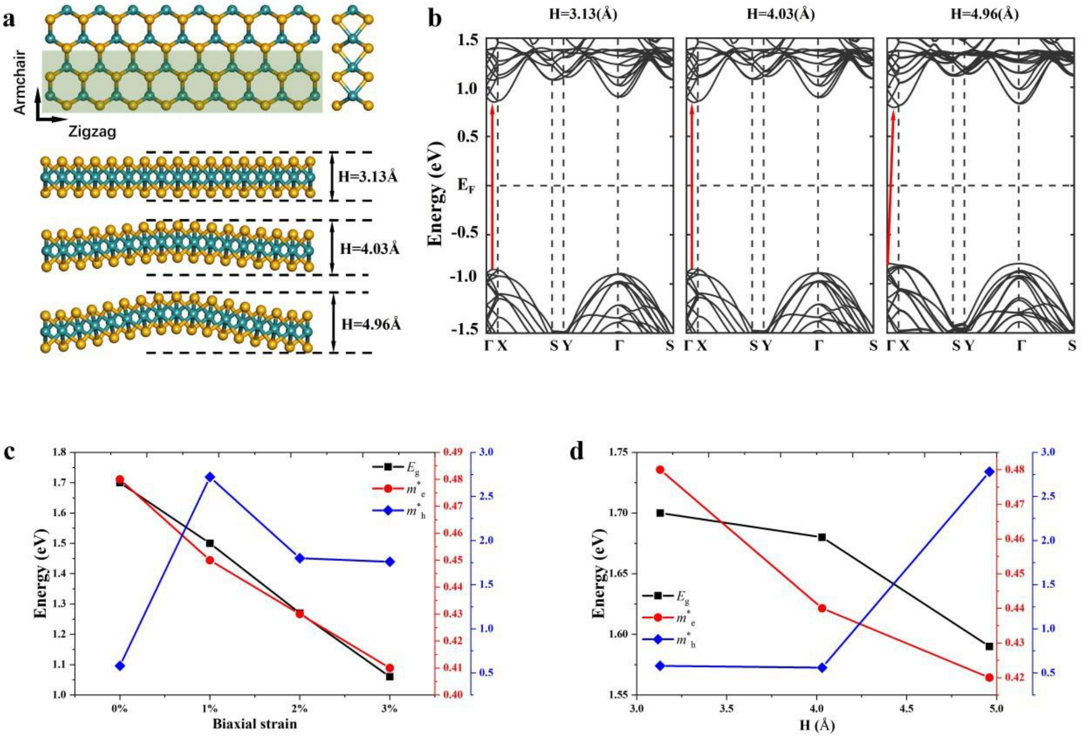

Fig. S15 (a) MoS_2 crystal structures with different bending heights for DFT calculation. (b) Band structure of monolayer MoS_2 with different bending heights. (c) Band gap, electron and hole effective mass of monolayer MoS_2 with different biaxial strains calculated by band structure. (d) Band gap, electron and hole effective mass of monolayer MoS_2 with different bending heights calculated by band structure.

Fig. S11(a-b) shows the crystal structure of monolayer MoS_2 with different bending heights for DFT calculations and draws its band structure, where the bending height with 3.13 Åis for the relaxed structure . Through the analysis and calculation of the band structure, we got the changes of band gap, electron and hole effective mass of MoS_2 under different biaxial strain and different bending height (Fig. S11(c-d)). It indicated that the band gap and electron effective mass of MoS_2 decrease with the increase of strain, whether caused by biaxial strain or bending. This corresponds to our PL spectral and electrical performance measurements.

Table S1. Field effect mobility and carrier concentration of different MoS_2 FETs.

	MoS_2	NPs/MoS_2	LSICD1 NPs/MoS_2	LSICD3 NPs/MoS_2
Mobility ($cm^2V^{-1}s^{-1}$)	1.9	36.1	44.1	39.5
Carrier concentration ($\times 10^{12}$ cm^{-2})	7.86	8.33	8.57	8.51

Table S2 Statistics of μ_{FE} of monolayer MoS_2 FETs grown by CVD

MoS_2	**Configurations**	**Dielectrics**	**μ_{FE}(cm^2V^{-1} s^{-1})**	**Ref.**
Monolayer by MOCVD	Back-gated	SiO_2	0.47	[7]
Monolayer by MOCVD	Back-gated	SiO_2	7-12	[8]
Monolayer by CVD	Back-gated	SiO_2	6.3-11.4	[9]
Monolayer by Au-assisted exfoliation	Top-gated	SiO_2	22.1-32.7	[10]
Monolayer by CVD	Back-gated	SiO_2	~40	[11]
Monolayer by CVD	Back-gated	SiO_2	1.2	[12]
Monolayers on Au by CVD	Back-gated	SiO_2	~11.2	[13]
Continuous monolayer by CVD	Back-gated	SiO_2	~9.8	[14]
Monolayer by MOCVD	Back-gated	SiO_2	21.6	[15]
Monolayers by VLS	Back-gated	SiO_2	21.1	[16]
Monolayer by CVD	Back-gated	SiO_2	2.87	[17]
Monolayer by MOCVD	Back-gated	SiO_2	21.6	[18]
Monolayer by VLS	Back-gated	SiO_2	33	[19]
Monolayer by CVD	Back-gated	SiO_2	1.9	
M@MO NPs/MoS_2	Back-gated	SiO_2	36.1	This work
LSICD M@MO NPs/MoS_2	Back-gated	SiO_2	44.1	

References

(1) PLIMPTON, S. FAST PARALLEL ALGORITHMS FOR SHORT-RANGE MOLECULAR-DYNAMICS. *J. Comput. Phys.* **1995**, *117* (1), 1–19. https://doi.org/10.1006/jcph.1995.1039.

(2) Kresse, G.; Furthmüller, J. Efficient Iterative Schemes for Ab Initio Total-Energy Calculations Using a Plane-Wave Basis Set. *Phys. Rev. B* **1996**, *54* (16), 11169–11186. https://doi.org/10.1103/PhysRevB.54.11169.

(3) Blöchl, P. E. Projector Augmented-Wave Method. *Phys. Rev. B* **1994**, *50* (24), 17953–17979. https://doi.org/10.1103/PhysRevB.50.17953.

(4) Perdew, J. P.; Burke, K.; Ernzerhof, M. Generalized Gradient Approximation Made Simple. *Phys. Rev. Lett.* **1996**, *77* (18), 3865–3868. https://doi.org/10.1103/PhysRevLett.77.3865.

(5) Monkhorst, H. J.; Pack, J. D. Special Points for Brillouin-Zone Integrations. *Phys. Rev. B* **1976**, *13* (12), 5188–5192. https://doi.org/10.1103/PhysRevB.13.5188.

(6) Hestenes, M. R.; Stiefel, E. Methods of Conjugate Gradients for Solving. *J. Res. Natl. Bur. Stand. (1934).* **1952**, *49* (6), 409.

(7) Kim, T.; Mun, J.; Park, H.; Joung, D.; Diware, M.; Won, C.; Park, J.; Jeong, S.-H.; Kang, S.-W. Wafer-Scale Production of Highly Uniform Two-Dimensional $MoS_2$by Metal-Organic Chemical Vapor Deposition. *Nanotechnology* **2017**, *28* (18), 18LT01. https://doi.org/10.1088/1361-6528/aa6958.

(8) Mun, J.; Park, H.; Park, J.; Joung, D.; Lee, S.-K.; Leem, J.; Myoung, J.-M.; Park, J.; Jeong, S.-H.; Chegal, W.; Nam, S.; Kang, S.-W. High-Mobility MoS2 Directly Grown on Polymer Substrate with Kinetics-Controlled Metal–Organic Chemical Vapor Deposition. *ACS Appl. Electron. Mater.* **2019**, *1* (4), 608–616. https://doi.org/10.1021/acsaelm.9b00078.

(9) Yang, P.; Zou, X.; Zhang, Z.; Hong, M.; Shi, J.; Chen, S.; Shu, J.; Zhao, L.; Jiang, S.; Zhou, X.; Huan, Y.; Xie, C.; Gao, P.; Chen, Q.; Zhang, Q.; Liu, Z.; Zhang, Y. Batch Production of 6-Inch Uniform Monolayer Molybdenum Disulfide Catalyzed by Sodium in Glass. *Nat. Commun.* **2018**, *9* (1), 979. https://doi.org/10.1038/s41467-018-03388-5.

(10) Huang, Y.; Pan, Y.-H.; Yang, R.; Bao, L.-H.; Meng, L.; Luo, H.-L.; Cai, Y.-Q.; Liu, G.-D.; Zhao, W.-J.; Zhou, Z.; Wu, L.-M.; Zhu, Z.-L.; Huang, M.; Liu, L.-W.; Liu, L.; Cheng, P.; Wu, K.-H.; Tian, S.-B.; Gu, C.-Z.; Shi, Y.-G.; Guo, Y.-F.; Cheng, Z. G.; Hu, J.-P.; Zhao, L.; Yang, G.-H.; Sutter, E.; Sutter, P.; Wang, Y.-L.; Ji, W.; Zhou, X.-J.; Gao, H.-J. Universal Mechanical Exfoliation of Large-Area 2D Crystals. *Nat. Commun.* **2020**, *11* (1), 2453. https://doi.org/10.1038/s41467-020-16266-w.

(11) Yu, H.; Liao, M.; Zhao, W.; Liu, G.; Zhou, X. J.; Wei, Z.; Xu, X.; Liu, K.; Hu, Z.; Deng, K.; Zhou, S.; Shi, J.-A.; Gu, L.; Shen, C.; Zhang, T.; Du, L.; Xie, L.; Zhu, J.; Chen, W.; Yang, R.; Shi, D.; Zhang, G. Wafer-Scale Growth and Transfer of Highly-Oriented Monolayer MoS2 Continuous Films. *ACS Nano* **2017**, *11* (12), 12001–12007. https://doi.org/10.1021/acsnano.7b03819.

(12) Durairaj, S.; Krishnamoorthy, P.; Raveendran, N.; Ryu, B. D.; Hong, C.-H.; Seo, T. H.; Chandramohan, S. Barrier-Assisted Vapor Phase CVD of Large-Area MoS2 Monolayers with High Spatial Homogeneity. *Nanoscale Adv.* **2020**, *2* (9), 4106–4116. https://doi.org/10.1039/D0NA00524J.

(13) Yang, P.; Zhang, S.; Pan, S.; Tang, B.; Liang, Y.; Zhao, X.; Zhang, Z.; Shi, J.; Huan, Y.; Shi, Y.; Pennycook, S. J.; Ren, Z.; Zhang, G.; Chen, Q.; Zou, X.; Liu, Z.; Zhang, Y. Epitaxial Growth of Centimeter-Scale Single-Crystal MoS2 Monolayer on Au(111). *ACS Nano* **2020**, *14* (4), 5036–5045. https://doi.org/10.1021/acsnano.0c01478.

(14) Lim, Y.-F.; Priyadarshi, K.; Bussolotti, F.; Gogoi, P. K.; Cui, X.; Yang, M.; Pan, J.; Tong, S. W.; Wang, S.; Pennycook, S. J.; Goh, K. E. J.; Wee, A. T. S.; Wong, S. L.; Chi, D. Modification of Vapor Phase Concentrations in MoS2 Growth Using a NiO Foam Barrier. *ACS Nano* **2018**, *12* (2), 1339–1349. https://doi.org/10.1021/acsnano.7b07682.

(15) Cun, H.; Macha, M.; Kim, H.; Liu, K.; Zhao, Y.; LaGrange, T.; Kis, A.; Radenovic, A. Wafer-Scale MOCVD Growth of Monolayer MoS2 on Sapphire and SiO2. *Nano Res.* **2019**, *12* (10), 2646–2652. https://doi.org/10.1007/s12274-019-2502-9.

(16) Li, S.; Lin, Y.-C.; Liu, X.-Y.; Hu, Z.; Wu, J.; Nakajima, H.; Liu, S.; Okazaki, T.; Chen, W.; Minari, T.; Sakuma, Y.; Tsukagoshi, K.; Suenaga, K.; Taniguchi, T.; Osada, M. Wafer-Scale and Deterministic Patterned Growth of Monolayer MoS2via Vapor–Liquid–Solid Method. *Nanoscale* **2019**, *11* (34), 16122–16129. https://doi.org/10.1039/C9NR04612G.

(17) Chee, S.-S.; Ham, M.-H. Low-Damaged Layer-by-Layer Etching of Large-Area Molybdenum Disulfide Films via Mild Plasma Treatment. *Adv. Mater. Interfaces* **2020**, *7* (17), 2000762. https://doi.org/https://doi.org/10.1002/admi.202000762.

(18) Xu, X.; Zhang, C.; Hota, M. K.; Liu, Z.; Zhang, X.; Alshareef, H. N. Enhanced Quality of

Wafer-Scale MoS2 Films by a Capping Layer Annealing Process. *Adv. Funct. Mater.* **2020**, *30* (11), 1908040. https://doi.org/https://doi.org/10.1002/adfm.201908040.

(19) Chang, M.-C.; Ho, P.-H.; Tseng, M.-F.; Lin, F.-Y.; Hou, C.-H.; Lin, I.-K.; Wang, H.; Huang, P.-P.; Chiang, C.-H.; Yang, Y.-C.; Wang, I.-T.; Du, H.-Y.; Wen, C.-Y.; Shyue, J.-J.; Chen, C.-W.; Chen, K.-H.; Chiu, P.-W.; Chen, L.-C. Fast Growth of Large-Grain and Continuous MoS2 Films through a Self-Capping Vapor-Liquid-Solid Method. *Nat. Commun.* **2020**, *11* (1), 3682. https://doi.org/10.1038/s41467-020-17517-6.